CHAPTER 5. SPATIOTEMPORAL EDGE EFFECTS ON A Pt RIBBON

5.1 Introduction

While on a ring electrode, studied in the last chapter, all locations are equivalent by symmetry, additional effects come into play on electrodes where this is not the case. Therefore in this chapter a thin ribbon electrode will be studied, where points at the centre are at a different state than points at the edges, which is expected to lead to a spatially inhomogeneous stationary state, but should also have an impact on spatiotemporal pattern formation. Since the mathematical derivation and theoretical calculations associated with the edge effect on ribbon electrode are similar to those on the disc electrode (which was already introduced by J. Christoph [27]), a brief mathematical description for a ribbon electrode will be given. An electrode with the length of L and the width of W is employed as the working electrode. The longer direction is the x-axis, as shown in Figure 5.1.

$$\tilde{x} \in [0,\ L],\ \tilde{y} \in [-W/2, W/2]$$

$$\Rightarrow \quad x \in [0,\ 1]\ (0 \le x \le 1),\ \ y \in [-b/2, b/2] \tag{5.1}$$

$$\text{with } b \equiv W/L \le 1,\ \ A_{WE} = L \times W,$$

where A_{WE} is the area of the working ribbon electrode and b is defined as W/L.

Thus, the electrode is quadratic when b is close to 1. When the width (W) of the rectangular electrode is very small ($b << 1$), WE corresponds to a thin ribbon electrode. In this case, as with the thin ring electrode, we do not have to consider the pattern

formation or the change of the double layer potential along the y-axis, since the pattern formation along the y-axis can be neglected.

Figure 5.2 shows the distribution of the double layer charge at the central horizontal line of the ribbon electrode and the double layer charge at two edges marked with dotted circles is monotonously increasing. When b is equal to 1 (quadratic shape), the maximum value of current density can be obtained at four edges (see Ref. [27] for details). However, the inhomogeneity of the double layer potential is mainly decreasing along the y-axis when the width (W) becomes smaller. Therefore, as b approaches 0, the inhomogeneity along the x-axis diminishes.

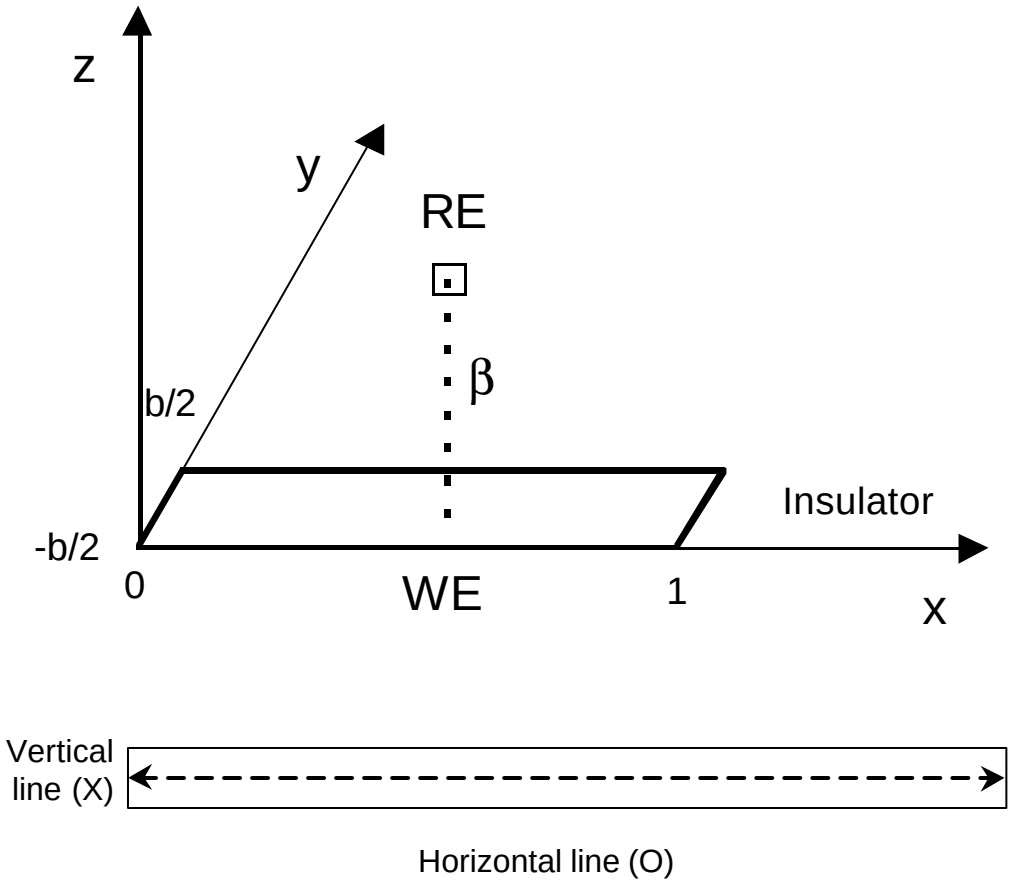

Figure 5.1. Geometry of the ribbon electrode when the reference electrode is located far away from it ($\beta \to \infty$). β is the parameter depending on the distance between WE and RE. A thin ribbon electrode with small width is used to investigate the horizontal edge effect.

The change of the double layer potential can be simplified and worded in one-dimensional double layer dynamics as in Eq. (5.2) (cf. Eq. (9) in Ref. [14]),

$$\partial_t u(x,\ t) = -i_r[u] + ?\ h(x)\ (E_0 - u) + ?\int_0^1 H_0(x,\ x')\ (u(x') - u(x))dx', \qquad (5.2)$$

where both the coupling function $H_0(x,\ x')$ and the local function $h(x)$ are explicitly position dependent. The mathematical derivation of these functions for a thin ribbon electrode is extensively described in Ref. [27].

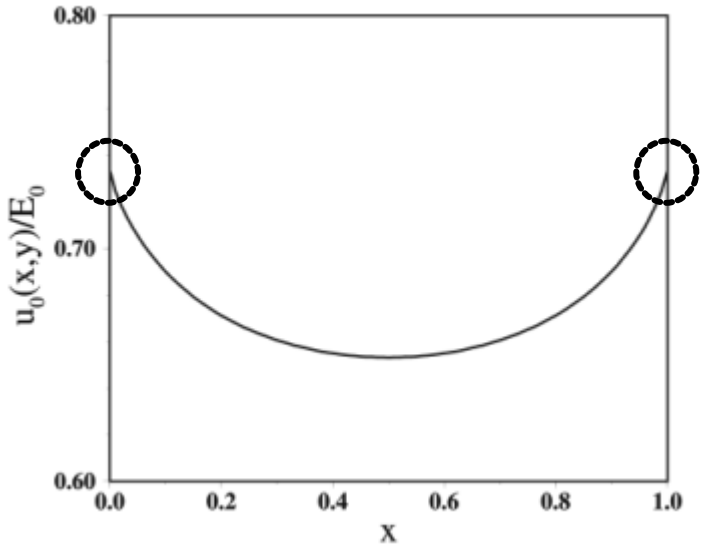

Figure 5.2. Double layer charge of a thin ribbon electrode by a linear reaction current ($\kappa / \mu = 1$). Double layer potentials, $u_0(x, y)$ or $i_{mig}(x, y)$ are both increasing to the edge of the x position ($x \rightarrow 0$ or 1). Thus, the maximum of current density is obtained at the two edges (x = 0 and 1). Courtesy of J. Christoph [27].

Figure 5.3 shows that the local coupling function of the effective spatial resistance also diverges at the edge of the electrode. Spatial resistance changes according to following equation:

$$\rho_{ele}(x) \equiv \frac{1}{\kappa h(x)}, \quad \rho_{ele}^{M} = \frac{1}{\kappa < h(x) >}. \qquad (5.3)$$

Here the smaller spatial resistance is only noticeable at the edge and it results in higher migration current at the edge region compared with the centre of the ribbon electrode.

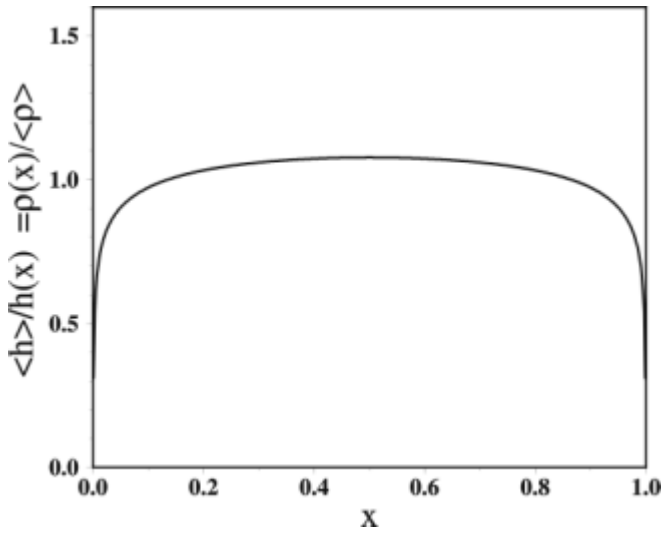

Figure 5.3. The inverse of the local function $< h >/h$ (x) of the three-dimensional coupling function (see Eq. (5.3)). b is 0.01. Courtesy of J. Christoph [27].

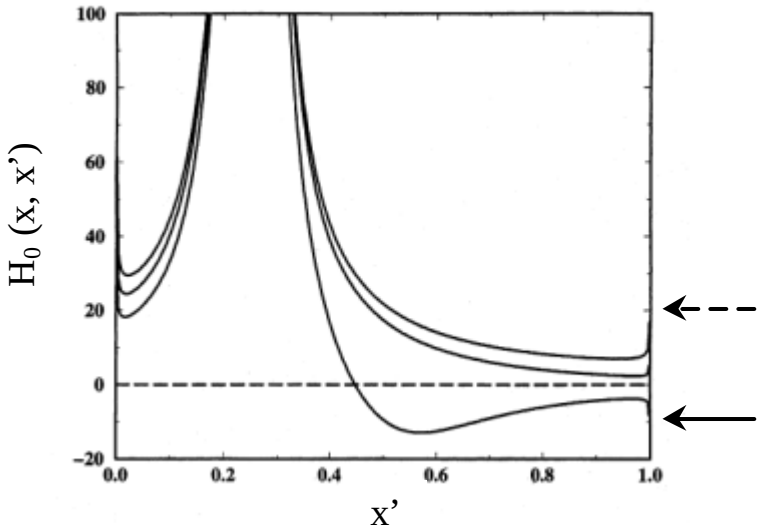

Figure 5.4. Where b (= B / L) is 0.01, coupling function H_0 (x, x') at x = 0.25. (a) Large and (b) small distances between WE and RE. Dotted and solid arrows indicate positive and negative coupling, respectively. Courtesy of J. Christoph [27].

As shown in Figure 5.4, potential coupling presents nonlocal coupling and it decreases as the distance between two coupled electrode points increases. However, the coupling diverges at the edges; *i.e.*, these tend to couple more strongly. Dotted and solid arrows in Figure 5.4 indicate the positive coupling and the negative coupling, respectively. These two different profiles of H_0 are due to several reasons, mostly to the different position of RE over the ribbon WE.

5.2 Experiments

Figure 5.5 shows the gas-tight, three-electrode and one-compartment arrangement for the measurement of local potential distributions at electrochemical interfaces. The electrochemical cell body consisted of a glass **cuboid** capped with a Teflon lid holding all electrodes (see Figure 5.5(a)). A polycrystalline Pt ribbon with a length of 58.0 mm and with a width of 4.0 mm (thickness of 0.1 mm) was used as working electrode (WE). Thus, the geometric area of the WE was 4.7 cm^2. Prior to each experiment, nitrogen bubbling is applied to remove dissolved oxygen (see four gas inlet parts of the Figure 5.5(b)).

Two Pt coils with a thickness of 1 mm were used as counter electrodes and placed far away from the WE ribbon electrode. The tip of a Luggin-Haber capillary hosting a Hg/Hg_2SO_4, saturated K_2SO_4 reference electrode was placed in the centre of the ribbon WE. Eight reference electrodes were equally distributed at about 0.8 mm distance from the WE in order to monitor the local interfacial potential, as shown in Figure 5.5(c). Figure 5.5(d) is the photo of the experimental setup.

All the solutions used in this chapter were prepared with ultrapure water (Millipore Milli-Q water, 18 $M\Omega \cdot cm$). Chemical and electrochemical pre-treatment and post-treatment of the ribbon working electrode was the same as that of the ring electrode (see Chapter 4) to confirm the absence of any residual surface impurities. The electrolyte was 0.1 M HCOONa in 0.033 M H_2SO_4 (bulk solution pH = 2.85).

An in-house-built potentiostat (*ELAB* of Fritz-Haber-Institut) was used for all cyclic voltammetry (CV) experiments and the data were transferred to an IBM compatible PC controlled by a GPIB interface.

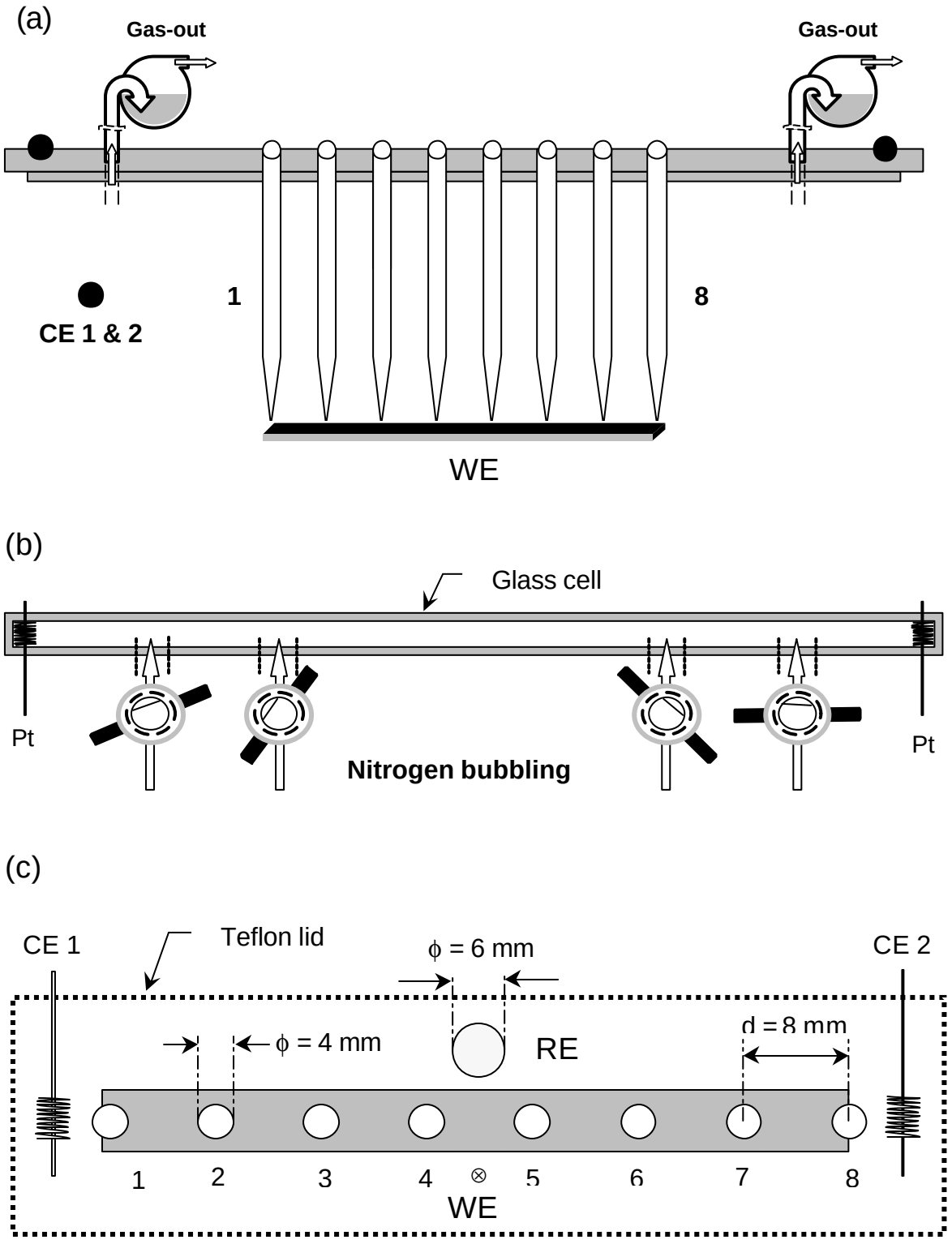

Figure 5.5. Schematic diagram of an experimental setup for the investigation of the edge effect on a ribbon electrode. (a) Side view, (b) top view and (c) detailed geometric drawing of three-electrodes used.

(d)

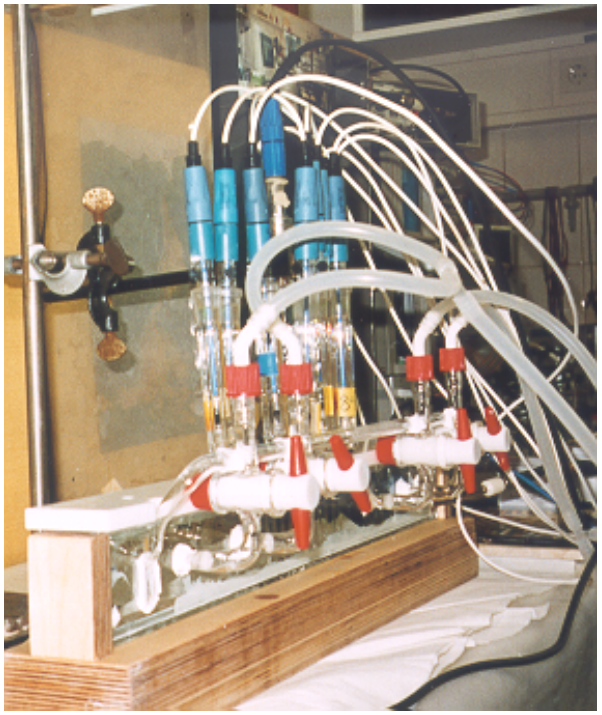

Figure 5.5. (Colour) (d) Photograph of experimental setup shows a ribbon working electrode (WE), two counter electrodes (CEs), a reference electrode (RE), eight microprobes (MP) and a glass capillary (GC) in the rectangular-shaped glass cell.

5.3 Edge effect in the bistable region

First of all, experimental observations of edge effects in bistable systems will be explained. Bistable media consist of elements that have two steady states, which stable under sufficiently small perturbations. Strong perturbations can cause transitions between these states. The fundamental form of a pattern in bistable media is a trigger wave, which represents a propagating front of transition from one stationary state into the other. The propagation velocity of a flat front is uniquely determined by the properties of the bistable medium. To initiate a spreading wave of transition from a homogeneous steady state, one should create a local perturbation which exceeds a critical threshold of the bistable medium. Such wave fronts were first observed in 1906 in a chemical reacting medium by R. Luther [171], who also made theoretical estimates

of their propagation velocity. Their detailed mathematical description was given in 1937 by P. Fischer [172], who studied a problem in population genetics, and one year later by Zeldovich and Frank-Kamenetskii [173] in the theory of flame propagation. Trigger waves are widespread phenomena, both in conservative systems such as ripples on the surface of water and in dissipative systems such as active chemical media [174], nerve axons, or heat tissues [175]. They typically originate from the location where a perturbation trigger has been applied, be it a stone thrown into a pond or an electrical stimulus applied to an axon. Strasser *et al.* [22, 144] experimentally and theoretically demonstrated the bistability in formic acid oxidation on several different single crystalline Pt electrodes. Recently, Christoph *et al.* presented remote triggering of waves in electrochemical oxidation of a formic acid system under bistable conditions [21, 27].

Figure 5.6 shows a typical current-potential profile for formic acid oxidation during the positive and negative directions scans on a polycrystalline Pt working electrode with a scan rate of 10 mV/s. The anodic peaks in the CV correspond to the oxidation of HCOOH in the course of both anodic and cathodic sweeps of the electrode potential. The fall of the current after the peak at +280 mV can be attributed to an increase in firmness of binding of the OH groups as the potential becomes more positive. This is associated with an increase in the OH-coverage, and a corresponding decrease in that of HCOOH.

On the negative going scan of the CV, a sharp and significant current peak (burst) appears, and this is attributed to renewed oxidation of the fuel. Since no reaction can occur at the electrode surface completely covered with oxygen, it is clear that part of the oxygen layer must first be reduced. Renewed anodic oxidation begins on the cathodic return between + 200 mV and 0.0 V, at a potential depending on the extent of the maximum oxygen coverage attained at the extreme of the preceding anodic scan, and on the velocity of potential change. This means that the current peak is displaced in the direction of the hydrogen potential. The current density is enhanced since the removal of oxygen has roughened and activated the surface.

Bistability of the current is obtained between + 190 mV and + 370 mV, which is subjected to the comparative study of inhomogeneous catalytic activity on the ribbon electrode on two different states, *i.e.*, active state (***a***) on the positive scan and passive state (***p***) on the negative scan.

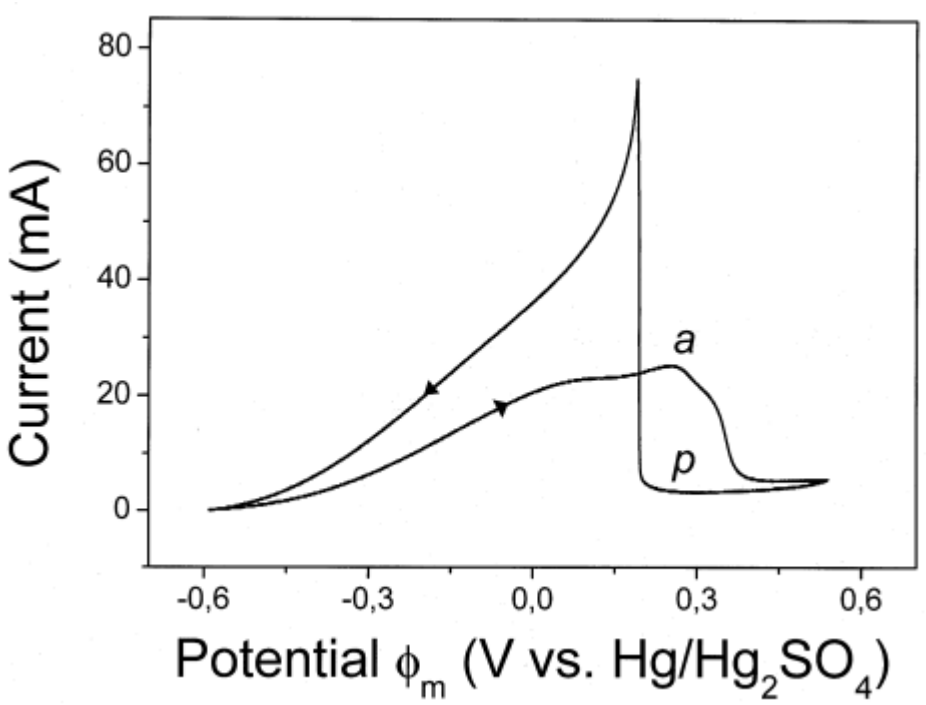

Figure 5.6. Cyclic voltammetry of a polycrystalline Pt working electrode with a scan rate of 10 mV/s. Solution is 0.1 M HCOONa/0.033 M H_2SO_4 in the absence of Bi ions. *a* and *p* indicate the active state and the passive state, respectively.

5.3.1 Bistable edge effect with different solution resistivity

According to theoretical simulations explained in section 5.1, there are two main observations induced by solution resistivity. At first, high solution conductivity induces the smaller edge effect between the active state and the passive state on the ribbon electrode and *vice versa*. It means that with increasing solution resistivity, much bigger inhomogeneity is obtained. Secondly, higher resistivity results in broader bistability, which can be shown during the transition from the active state to the passive state on the anodic scan, and this occurs at further outer potential compared with lower resistivity. On the cathodic scan in the CV measurement, autonomous transition from passive state to active state is observed at lower outer potential when the electrolyte with a high resistivity is used.

Figure 5.7 shows the theoretical and experimental bistable regions with different solution conductivities (or resistivities). Comparing with normal CV experiments, a

much slower scan rate of 1 mV/s is applied in order to avoid the hysteresis of the CV curve between both scans.

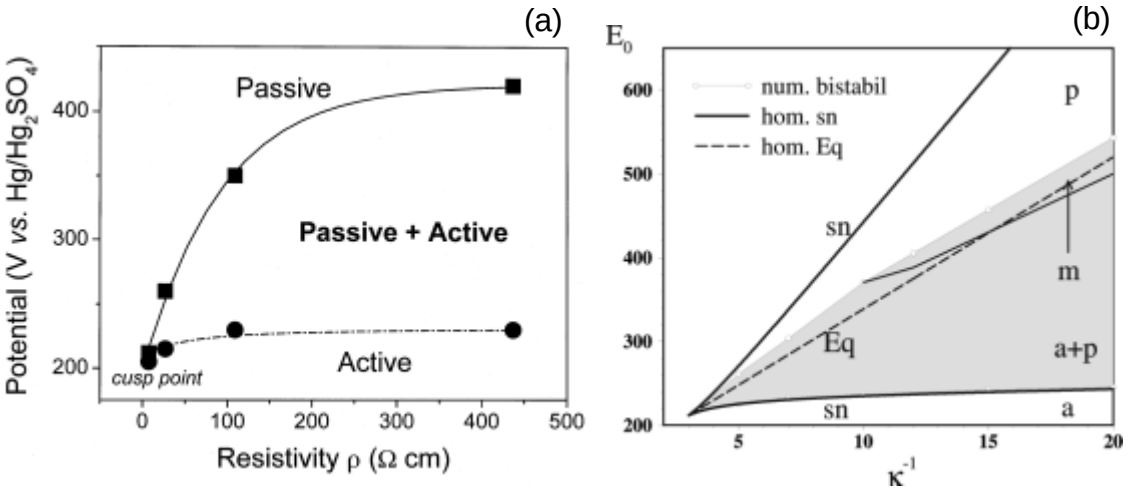

Figure 5.7. (a) Experimental data of a bistable region with different solution resistivities. (b) Theoretical bistable region (see gray part) and thick line indicate saddle-node bifurcation at **b** = 0.01 (Courtesy of J. Christoph [27]). Active state (a) changes into mixed state (a+p). E_0 is the outer potential and κ^{-1} is the reverse of the solution conductivity ($\kappa^{-1} \sim \rho$).

To summarise the experimental results so far, we plot the bifurcation curves in the E_0/ρ (or κ^{-1}) plane in Figure 5.7. At extremely low resistivity, *i.e.*, at highest solution conductivity, two saddle-node curves (passive to active and *vice versa*) meet tangentially and such a point is called a *cusp point*.

5.3.2 Spatiotemporal edge effect with different b

Figure 5.8 shows stationary potential distribution along the Pt ribbon electrode in the electrocatalytic oxidation of formic acid. These data were obtained in the bistable region on the anodic scan (a) and on the cathodic scan (b) as shown in Figure 5.6. In this case, the distance parameter β between WE and RE is 0.7. The definition of RE distance parameter β on the ribbon-shaped media is as follows:

Parameter b

$$\beta = \frac{d}{l}, \tag{5.4}$$

where **d** is the distance between WE and RE and **l** is the horizontal length of the ribbon-shaped WE.

RE far away from WE

According to the theory described in the above section 5.1, the inhomogeneous behaviour of the active state is relatively higher than that of the passive state. In other words, the edge of the ribbon tended to be in a more passive state (higher interfacial potential) compared with the centre. The absolute (or average) value of the interfacial potential of the passive state, however, is bigger than that of the active state (not shown in this work).

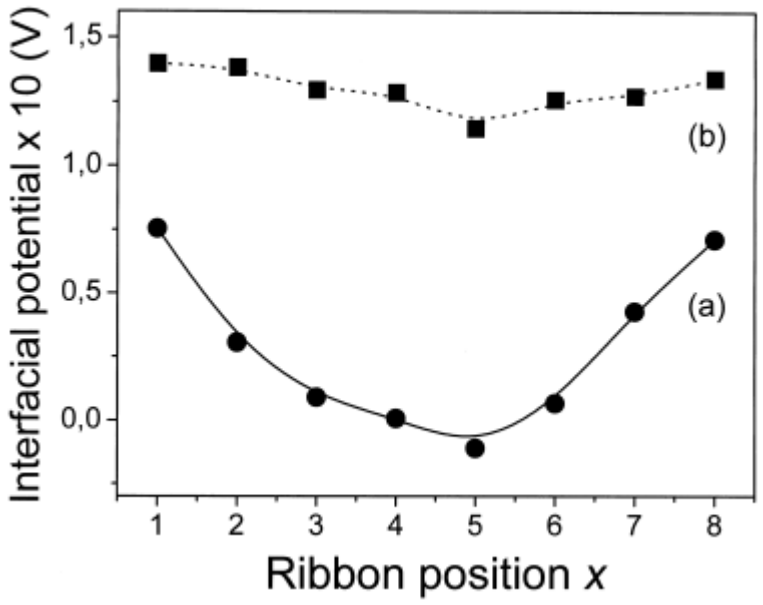

Figure 5.8. Experimental results of bistabiltiy at $\beta = 0.7$ (cf. Eq. (5.4)). Fixed outer potential (U_{fixed}) is + 290 mV. Eight microprobes were used in order to monitor the change of the double layer potential. Electrolyte is 0.1 M HCOONa/0.033 M H_2SO_4. (a) Active state and (b) passive state of bistable region.

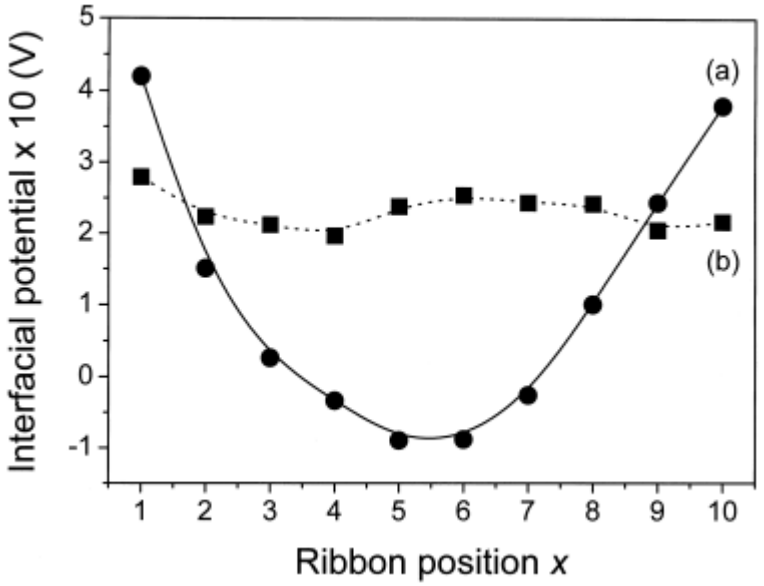

Figure 5.9. Distribution of the double layer potential at $\beta = 0.35$. U_{fixed} is + 290 mV. 0.1 M HCOONa/0.033 M H_2SO_4 without Bi^{3+}. (a) Active state and (b) passive state of bistable region.

On the other hand, when the distance between the WE and the RE decreases, negative nonlocal coupling should be considered to interpret the distribution of the interfacial potential as for the ring electrode (Chapter 4). At $\beta = 0.35$ (*i.e.*, 20 mm distance between WE and RE), one can clearly see a different profile along the ribbon electrode as shown in Figure 5.9. If there is no negative nonlocal coupling, the interfacial potential at two edges on the anodic scan (*i.e.*, active state (***a***) of the electrode) should not be higher than that of the passive state (see ***p*** in Figure 5.6). In Figure 5.9, we found that the interfacial potential on two edges of the ribbon electrode is higher than that at the passive state. However, the average value of the interfacial potential of the active state is smaller than that of the passive state.

5.3.3 Autonomous transitions

The bistability region is terminated by autonomous transitions. Activation fronts (at low potential) start from the middle of the ribbon electrode and passivation fronts (high potential) from the edges.

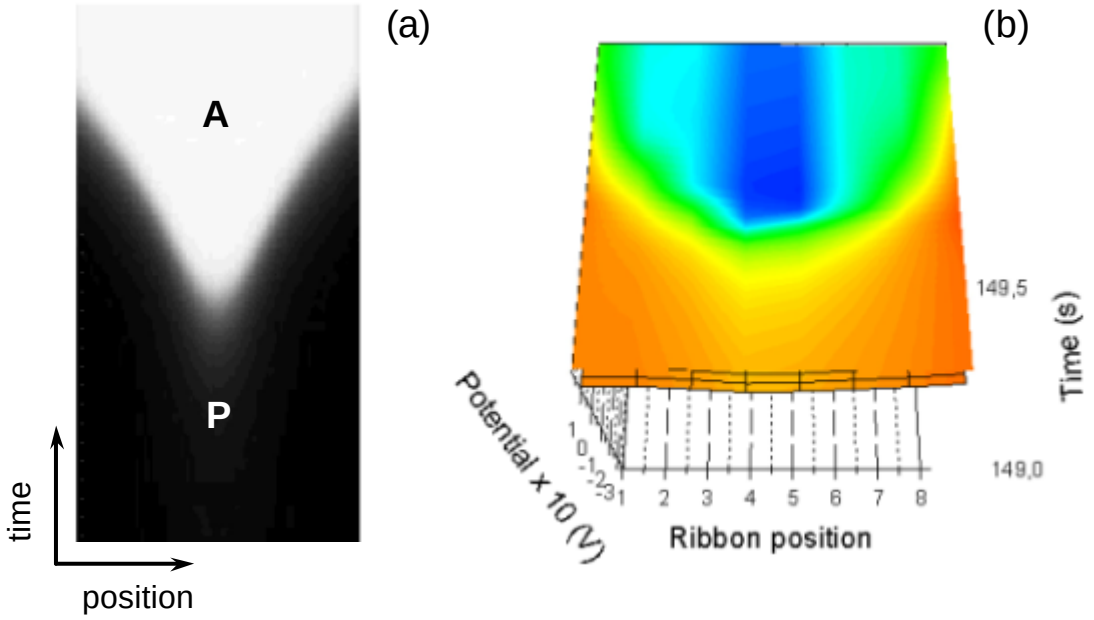

Figure 5.10. Autonomous transition from passivation (P) to activation (A) on a thin ribbon electrode is shown. Parameter as in Figure 5.7(b). (a) Theoretical simulation (black: passive state, white: active state) (Courtesy of J. Christoph [27]) and (b) (colour) experimental observation (blue: active state, red: passive state).

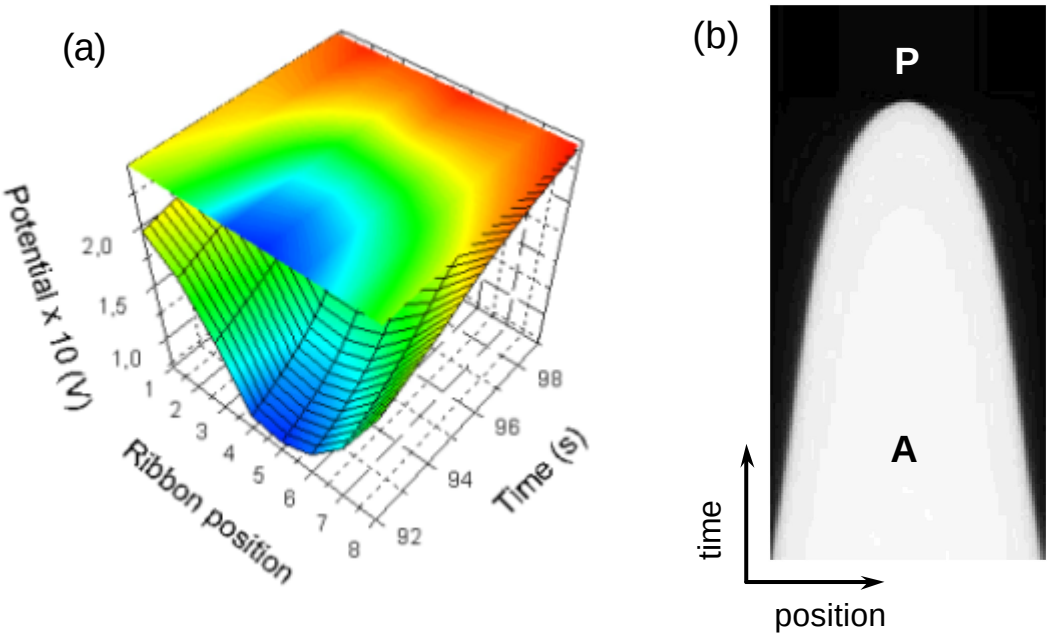

Figure 5.11. Autonomous transition from activation (A) to passivation (P) on a thin ribbon electrode is shown. (a) (Colour) experimental data (blue: active state, red: passive state) and (b) theoretical computer simulation (black: passive state, white: active state). Courtesy of J. Christoph [27].

As the outer potential was decreased, until the passive state became unstable, the active state first appeared in the middle of the ribbon working electrode and induced activation fronts spreading to the edges (Figure 5.10). Note that the front is accelerated as the activated area increases.

In contrast, at the other end of the bistable region passivation fronts started at both edges instantaneously and spread until they meet at the centre (Figure 5.11). Again the front velocity increases as the fronts spread.

5.3.4 Asymmetric edge effect

The two counter electrodes, CE 1 and CE 2, are generally located well above (200 mm) the WE ribbon electrode in order to avoid consideration of an unequal potential drop between CE and WE (see Figure 5.5). In other words, if CE 1 and CE 2 near two edges of the ribbon electrode are considered to be at infinity, asymmetric counter effect can be neglected. However, we should take into account asymmetric edge effect of the double layer potential on the ribbon when CEs are sufficiently close to WE.

Figure 5.12(a) shows the distribution of the interfacial potential on the anodic scan on a ribbon electrode where only CE 2 (near ribbon position 8) is connected. Comparing the asymmetric potential distribution, as shown in Figure 5.12(a) with the symmetric edge effect under bistable conditions (see Figure 5.8 or 5.10), the value of the interfacial potential at ribbon position 8 is about two times higher than the value of positions 1 and 8 in Figure 5.8 (or 5.10). This experimental observation can be readily explained by the following simple mathematical description (cf. Figure 5.12(b)).

$$\phi_{CE-WE} = \phi_{DL} + \phi_0 = \phi_{DL}(x) + \phi_0(x), \tag{5.5}$$

$$\phi_{CE-WE} = \phi_{DL}(x_1) + \phi_0(x_1) = \phi_{DL}(x_2) + \phi_0(x_2), \tag{5.6}$$

where ϕ_{CE-WE} are the potential difference between WE and CE, ϕ_{DL} and ϕ_0 (x) present the double layer potential and the potential drop in the electrolyte, respectively.

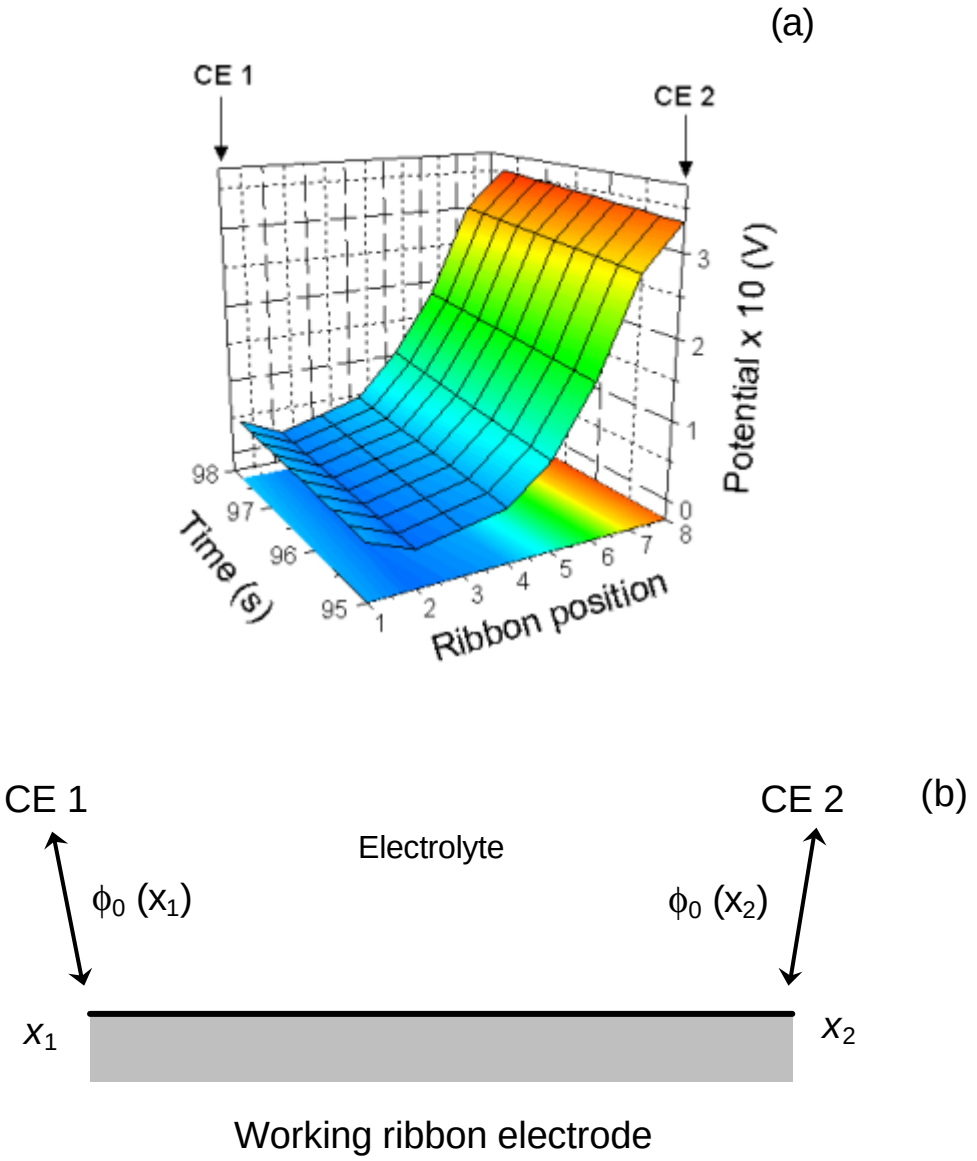

Figure 5.12. (Colour) (a) Interfacial potential distribution on a ribbon in bistable region as only CE 2 is connected. (b) Schematic drawing of ϕ (x) at two edges of the ribbon electrode.

When the potential drop ϕ_0 (x_1) at position 1 (x_1) is higher than the potential drop ϕ_0 (x_2) at position 2 (x_2), the double layer potential ϕ_{DL} (x_1) at position 1 is smaller than the interfacial potential ϕ_{DL} (x_2) at position 2. The larger distance to the counter electrode results in a larger potential drop in the electrode and it can induce a smaller double layer potential drop.

5.4 Edge effect under oscillatory conditions

5.4.1 Spatiotemporal edge oscillations with different b

Figure 5.13 shows a photograph of an experimental setup of another glass cell. The height of the glass cell is 250 mm and, with this glass, β can be increased up to 3.5, which was enough to study the potential distribution for strongly positive coupling. Eight microprobes were used in order to investigate the effect of positive and negative coupling occurring at the ribbon-shaped media.

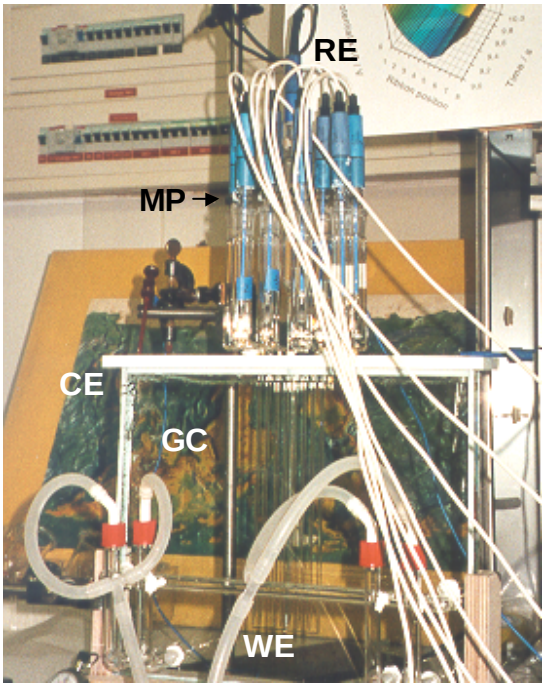

Figure 5.13. (Colour) Experimental setup shows the ribbon WE, two counter electrodes, reference electrode (RE), 8 microprobes (MP) and glass capillary (GC) in the cuboid cell.

Figure 5.14 shows the temporal signal of current oscillations during a cyclic voltammetry with a scan rate of 10 mV/s. The behaviour in the time domain displays small amplitude harmonic oscillations which become larger with increasing outer potential. Since the RE is placed at *ca.* 90 mm away from the WE (β = 1.50), the

potential range of current oscillations on the anodic scan as shown is relatively shorter than that at a small distance between the WE and the RE (see following Figure 5.17), and current oscillations are observed at positive current-potential slope. As already mentioned in Figure 5.7, lower conductivity induced a broader bistable region (see dotted arrow) due to a higher IR drop.

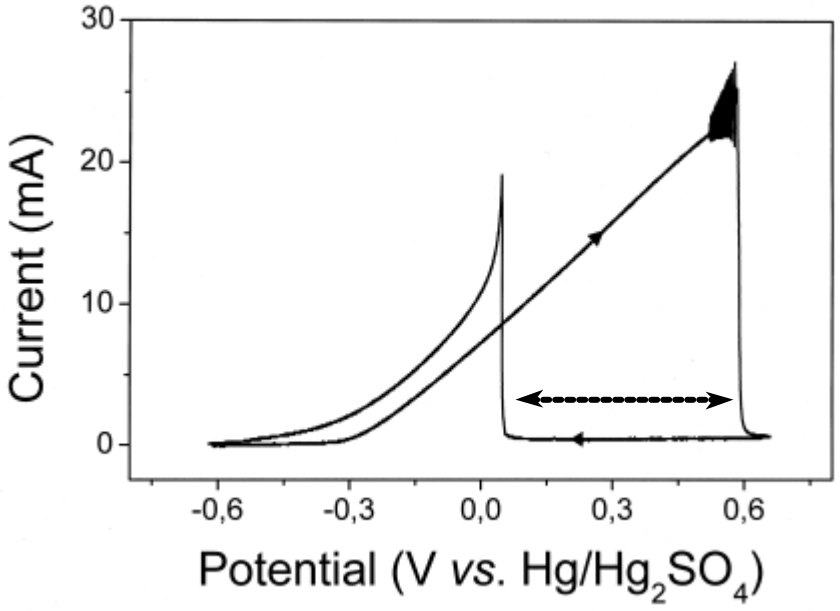

Figure 5.14. Cyclic voltammetry of a Pt working electrode modified by Bi deposition. Scan rate is 10 mV/s and solution is 0.1 M HCOONa/0.033 M H_2SO_4 with 1×10^{-6} M Bi^{3+}. β (d/l) is 1.50.

The spatial pattern and blow-up of temporal oscillations underlying the anodic scan of Figure 5.14 are reported in Figures 5.15 and 5.16. At the beginning of the oscillations, the distribution of the interfacial potential clearly represents in-phase edge oscillations (see Figure 5.15(b)) due to the global positive coupling as explained in Figure 5.3(a). With increasing outer potential, the oscillations penetrated more and more into the bulk of the electrode (Figure 5.16).

At the outer potential of + 600 mV, current oscillations died out as a result from the poisoning by oxygen species. Then the entire area of the electrode became passive (white domain at time = 119.8 s) and the anodic current dropped sharply as shown in Figure 5.16(a).

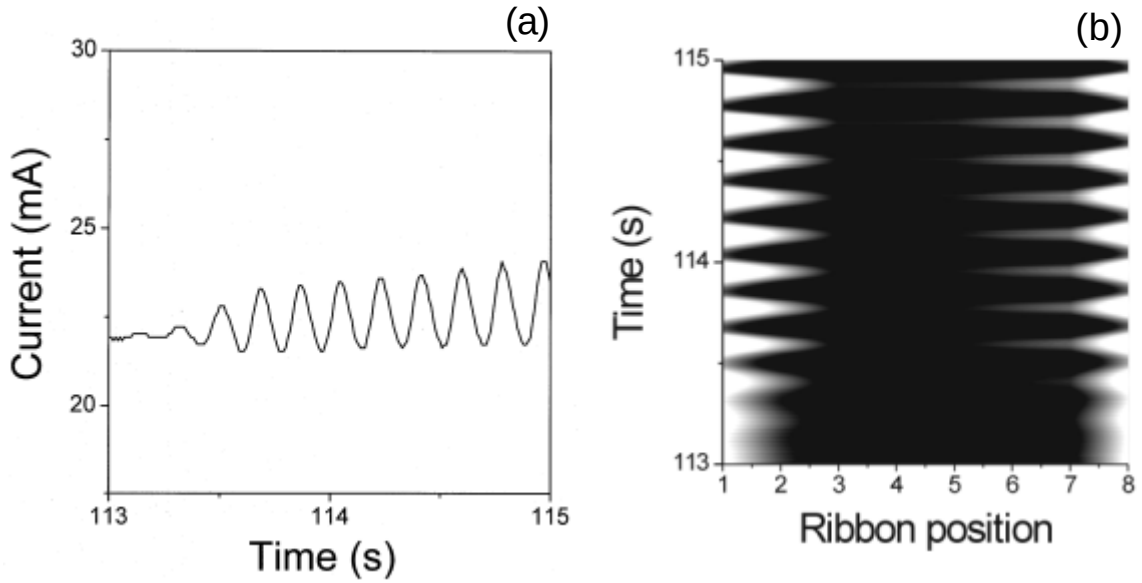

Figure 5.15. Edge oscillations at β = 1.50. (a) Temporal data and (b) spatiotemporal in-phase pattern formation near the beginning of current oscillations on the anodic scan in Figure 5.14. White and black colours indicate passive and active states, respectively.

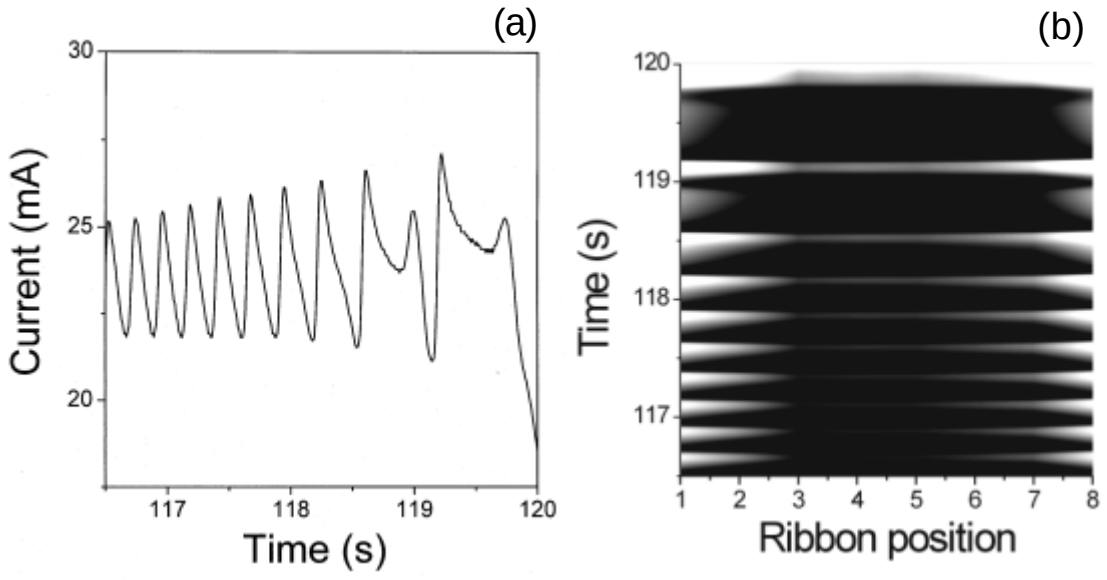

Figure 5.16. Edge oscillations at β = 1.50. (a) Spatiotemporal and (b) temporal current oscillations at the end of anodic current oscillations on the positive scan. White and black colours indicate passive and active states, respectively.

RE close to the WE

As the RE was located at *ca.* 20 mm ($\beta = 0.35$) above the ribbon WE, current oscillations were observed in a broader potential range from + 60 mV to + 450 mV; *i.e.*, current oscillations occur at an earlier overpotential compared with that at $\beta = 1.50$ (see Figure 5.14). The difference in oscillatory behaviour between Figures 5.14 and 5.17 results from a different uncompensated solution resistance (different IR drop) induced by the various distances between the WE and the RE. The potential parameter dependence of the current oscillations exhibits the following interesting features. Current oscillations with a small amplitude and a high frequency set in on the anodic scan. A stationary current-potential profile with a positive slope is obtained at a low overpotential, whereas a current-potential curve with negative differential resistance shows the higher amplitude and a smaller frequency oscillation at high anodic overpotential.

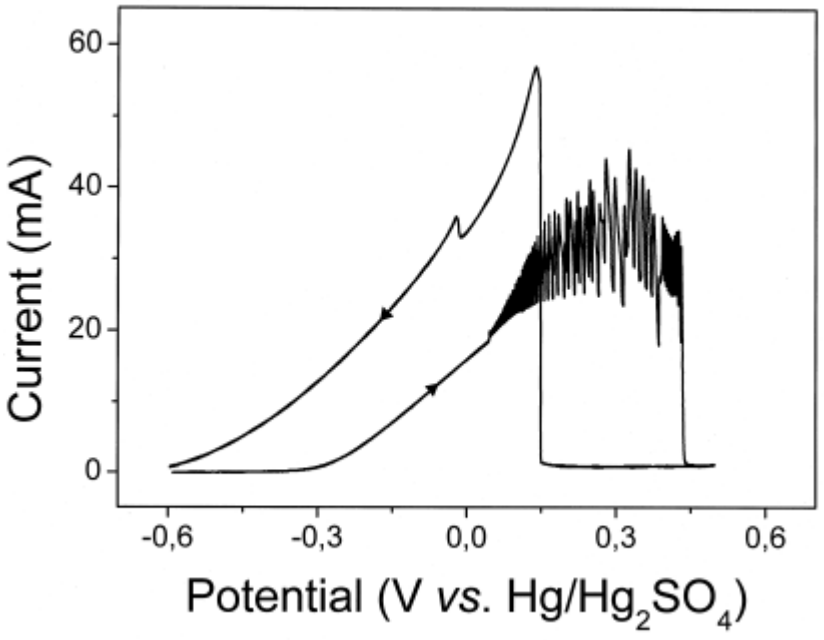

Figure 5.17. Cyclic voltammetry of a Pt ribbon electrode modified by Bi deposition. Scan rate is 10 mV/s and solution is 0.1 M HCOONa/0.033 M H_2SO_4 with 1×10^{-6} M Bi^{3+}. β is 0.35.

As discussed earlier in Chapter 4, the HCOOH oxidation on Bi/Pt can be categorised into the mechanistic class IV of HNDR oscillators. Far from the onset of oscillations, oscillations persist on a branch in the CV with NDR. The negative

differential resistance is due to increasing poisoning by O_{ad} with increasing potential, the slow negative feedback loop is most likely due to the transport of HCOOH to the electrode (see [57, 63] for details).

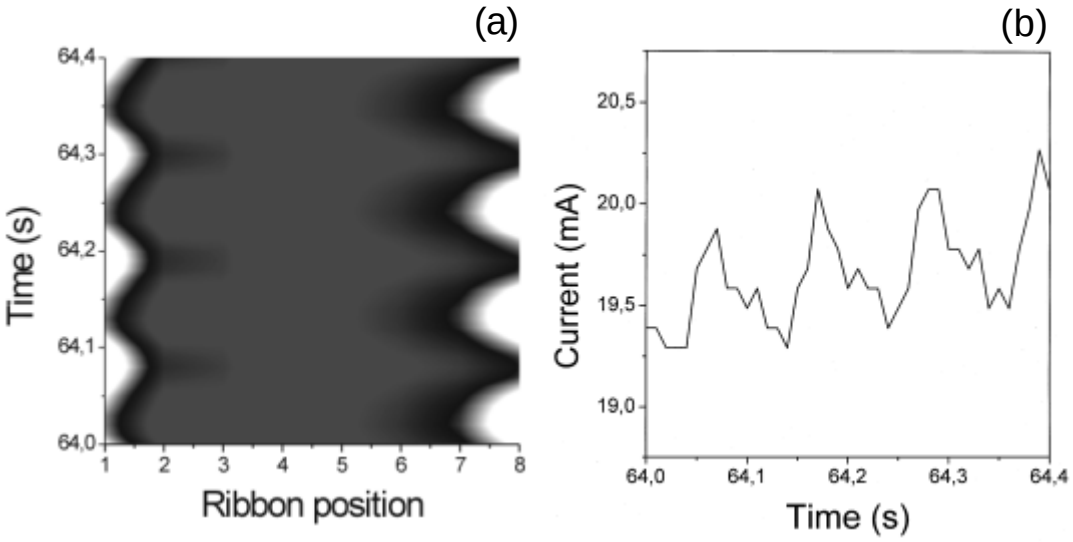

Figure 5.18. (a) Spatiotemporal anti-phase oscillations at $\beta = 0.35$ on the anodic scan in Figure 5.17. (b) Temporal current oscillations at the beginning of current oscillations. Electrolyte is 0.1 M HCOONa/0.033 M H_2SO_4 with 1×10^{-6} M Bi^{3+}.

The spatiotemporal interfacial potential pattern and detailed temporal oscillations corresponding to Figure 5.17 are extensively shown in Figures 5.18 to 5.20. At the onset of current oscillations, the distribution of the interfacial potential shows anti-phase edge oscillations as seen in Figure 5.18(a), since there exists negative long-range coupling (see Figure 5.3(b)).

Figure 5.19 shows period-doubled current oscillations with lower frequency compared with Figure 5.18(b). The passive state (white domain) at the two edges is asymmetrically approaching the centre. Unlike Figure 5.16(a), at higher potential of + 150 mV, anti-phase oscillations were observed with larger amplitude and smaller frequency (Figure 5.19(b)).

Near the termination of current oscillations on the anodic scan the oscillation cycles still started with passivation from the edges, but were generally strongly asymmetric (Figure 5.20). It is at present not clear, whether this is a result of a genuine symmetry-breaking transition, or whether the system just becomes more sensitive to a small deviation from a symmetric arrangement of the electrodes.

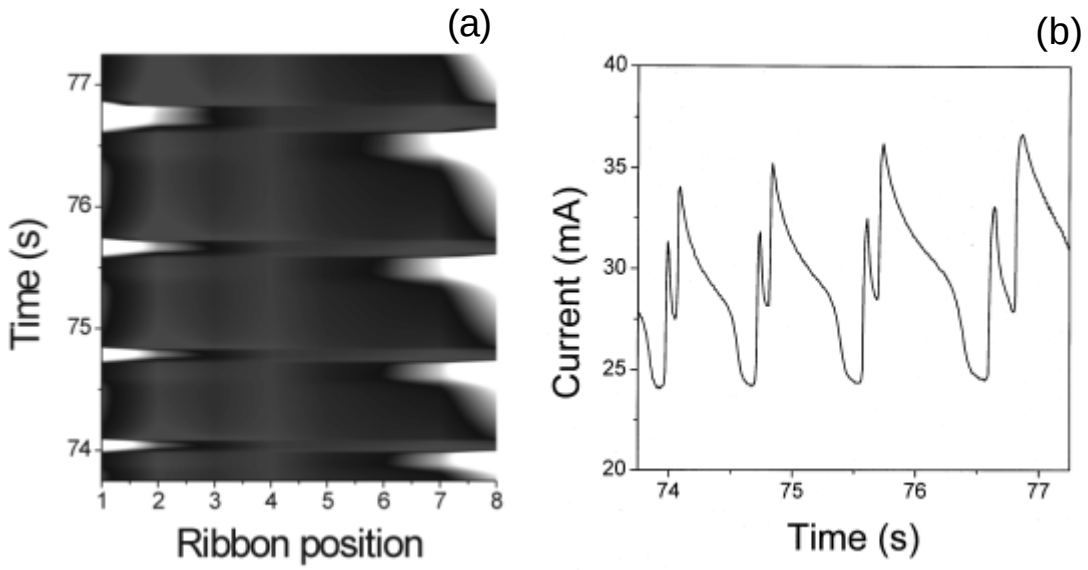

Figure 5.19. (a) Spatiotemporal distribution of the local interfacial potential at $\beta = 0.35$ and (b) temporal current oscillations at the middle of current oscillations on the anodic scan in Figure 5.17.

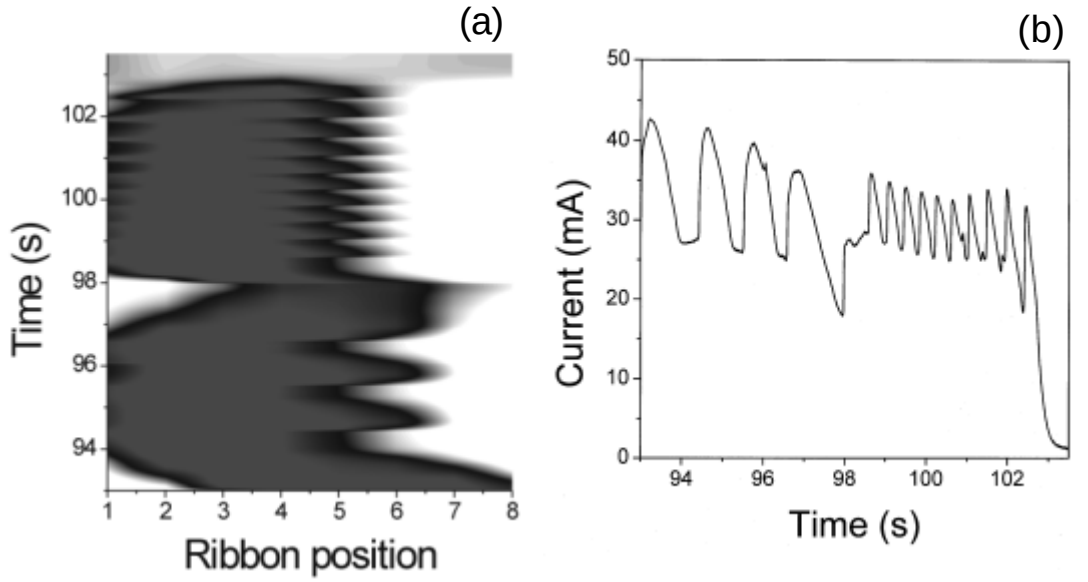

Figure 5.20. Edge oscillations at $\beta = 0.35$. (a) Spatiotemporal and (b) temporal current oscillations at the termination of current oscillations on the anodic scan.

5.5 Summary

While the previous Chapter 4 showed spatiotemporal pattern formation on a Pt **ring** electrode, recent relevant spatiotemporal data on a **ribbon-**shaped electrode are presented and compared with theoretical simulations developed by J. Christoph [27]. Experimental observations clearly prove the theoretical expectation derived from a reaction-migration equation.

The geometry of the ribbon electrode gives rise to edge effects of the interfacial potential in bistable systems. Under oscillatory conditions, during HCOOH oxidation on a Bi deposited Pt ribbon electrode anti-phase edge oscillations were observed on the anodic scan due to negative nonlocal coupling. On the other hand, in-phase edge oscillations were detected when the reference electrode was located far away from the working ribbon electrode.